Electronic Supplementary Material (ESI) for Nanoscale.

Electronic Supplementary Information: 'Towards Higher Electron Mobility in Modulation Doped GaAs/AlGaAs Core–Shell Nanowires'

Jessica L. Boland,[†] Gözde Tütüncüoglu,[‡] Juliane Gong,[†] Sonia Conesa-Boj,[¶] Christopher L. Davies,[†] Laura M. Herz,[†] Anna Fontcuberta i Morral,[‡] and Michael B. Johnston[*,†]

†*Department of Physics, University of Oxford, Clarendon Laboratory, Parks Road, Oxford, OX1 3PU, United Kingdom*

‡*Laboratory of Semiconductor Materials, École Polytechnique Fédérale de Lausanne (EPFL), CH-1015 Lausanne, Switzerland*

¶*Kavli Institute of Nanoscience, Delft, University of Technology Lorentzweg 1, 2628 CJ Delft The Netherlands*

E-mail: michael.johnston@physics.ox.ac.uk

Experimental Details

Nanowire Growth

For both samples, the GaAs nanowires were grown on a native oxide covered (111) Si substrate by the catalyst-free gallium assisted method in a DCA P600 solid source MBE system. For the modulation doped sample, growth of the GaAs core was carried out with a growth rate of 0.5 Å/s, a V/III ratio of 20 and a substrate temperature of 640°C. Prior to the growth of the AlGaAs shell, gallium flux has been cut for 20 minutes in order to consume the droplet, following which the growth is switched from axial to radial growth conditions by decreasing the substrate temperature to 495°C and increasing the V/III ratio to 80 by increasing the arsenic flux to 1.2×10^{-5} torr. The modulation doped sample is grown under a rotation of 15 rpm to increase uniformity, whereas the undoped core/shell sample is grown with 7 rpm. For the undoped sample, the GaAs core was grown at a rate of 0.3 Å/s, a V/III ratio of 40 and a substrate temperature of 640°C. The AlGaAs shell was grown by increasing the arsenic flux to 1.3×10^{-5} torr to give a V/III ratio of 100, and lowering the substrate temperature to 480°C. Thus, the growth conditions for both samples were very similar, showing that they are appropriate for comparison. All samples were transferred to z-cut quartz substrates. They were all rubbed in the same direction to align them with the nanowire axis parallel to the electric field polarisation. The fill factor for both samples was measured to be 80%, which is used in calculations in the manuscript. Due to the inhomogeneous averaging of the nanowire distribution, all the mobility values are underestimated.

Terahertz Time-Domain Spectroscopy

An amplified Ti:Sapphire laser with an average power of 4 W was used to generate 35 fs pulses centred at 800 nm at a repetition rate of 5 kHz. Each pulse was separated into three different paths: 590 μJ/pulse as an optical pump to photoexcite the sample; 200 μJ/pulse to generate the THz probe via optical rectification in a 2 mm GaP crystal; and 1.6 μJ/pulse as

a gate beam for electro-optical detection of the transmitted THz pulse via a 200 μm GaP crystal. The optical pump beam was attenuated by neutral density filters to photoexcite the nanowires at a range of fluences between 0.46 and 225 μJ cm^{-2}. At the sample, the full width half maximum (FWHM) for the optical pump beam is 10 mm and for the THz probe is 1 mm, so that the THz probe measures an area of homogenous photoexcited carrier density. The THz electric field, E, was measured using a balanced photodiode circuit and a lock-in amplifier referenced to a chopper at 2.5 kHz in the THz generation beam. The optical pump-induced change in the THz electric field, ΔE was measured using a second lock-in amplifier referenced to a chopper at 125 Hz in the optical pump beam. By varying the time delays between all three beams, a 2D map of the THz spectral response as a function of time after photoexcitation can then be measured. By also varying the power of the optical pump beam, a THz spectra response as a function of photoexcitation fluence can also be obtained. All measurements were taken at room temperature with the THz beam under vacuum to avoid any absorption of THz radiation by atmospheric water vapour. The sample was positioned in an Oxford Instruments cryostat to allow for THz photoconductivity data to be measured at a range of temperatures between 5 K and 300 K.

Time-Resolved Photoluminescence

An ultrafast pulsed Ti:Sapphire laser (100 fs pulse duration) tuned to 800 nm was used to photoexcite the nanowires with a range of fluences between 0.15 and 50 μJcm^{-2}. The emitted light was spectrally filtered (using a 880 nm $\pm$70 nm bandpass filter) to remove the residual scattered excitation pulse, and was focused onto the entrance slit of a liquid nitrogen cooled CCD detector conneced to a 160 mm spectrograph equipped with a 300 lines/mm grating. The photoluminescence (PL) spectra were corrected according to the spectral response of the apparatus. The sample was positioned in an Oxford Instruments cryostat to allow for PL spectra to be measured at a range of temperatures between 5 K and 300 K.

Simulations of Bandedge Profiles and Equilibrium Extrinsic Carrier Concentration Distribution for Modulation Doped Sample

Self-consistent numerical solutions of the Schrödinger and Poisson equations were performed on the modulation doped nanowire heterostructure shown in Figure S1a using the NextNano package[1] as described in Ref.[2] Figure S1b shows the equilibrium band-edge diagrams for the modulation doped nanowire structure at room temperature, with a clear bandbending resulting from the presence of the ionised Si-delta-doped layer in the AlGaAs shell. Figures S1c and d show that the donated electrons are transferred from the AlGaAs shell to the lower bandgap GaAs core region of the nanowire. From these simulations, an electron density of approximately $1.7\times10^{16}\,\mathrm{cm}^{-3}$ is expected in the GaAs core for a nominal doping density of $4.5\times10^{18}\,\mathrm{cm}^{-3}$ in the delta-doped layer.

Data Analysis of THz Transmission Data

Conversion of THz Transmission to Photoconductivity

The photoconductivity, $\Delta\sigma$, is extracted from the OPTP measurements of $\frac{\Delta E}{E}$. The nanowires are considered to be embedded within a surrounding layer of thickness, d, which is the average diameter of the nanowire; and to have an effective areal fill factor obtained from optical microscope images. The transmitted terahertz fields with and without the optical pump are described as follows:

$$E_{\mathrm{on}} = f_{\mathrm{w}} E_{\mathrm{w}*} + (1 - f_{\mathrm{w}})\, E_{\mathrm{v}} \tag{1}$$

$$E_{\mathrm{off}} = f_{\mathrm{w}} E_{\mathrm{w}} + (1 - f_{\mathrm{w}})\, E_{\mathrm{v}} \tag{2}$$

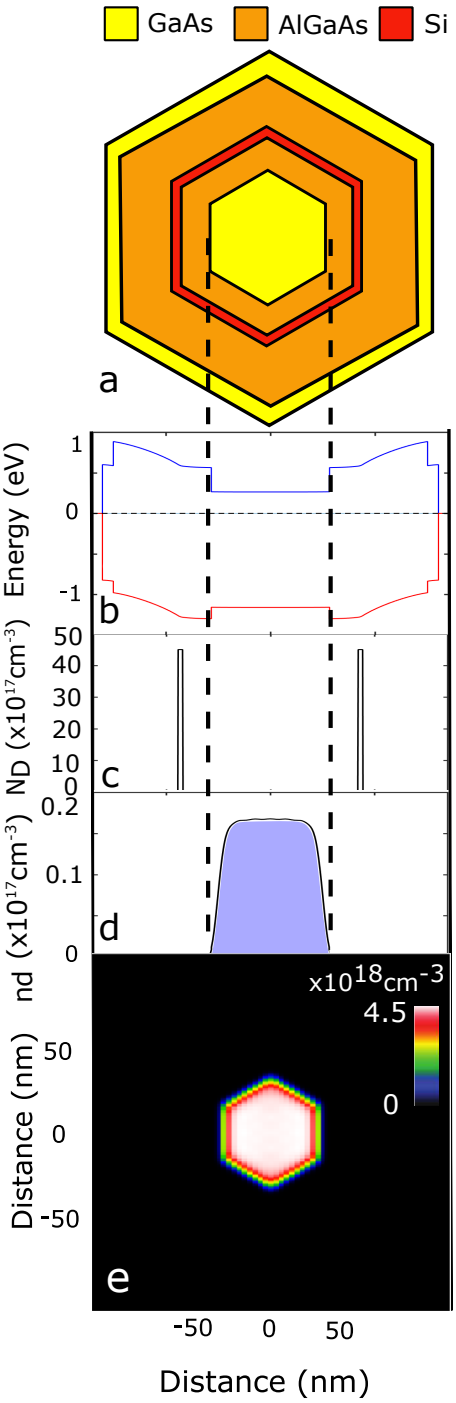

Figure S1: (a) Schematic diagram of modulation doped nanowire. (b) Simulated energy band diagram for the modulation doped GaAs/AlGaAs nanowires with donors fully ionised ($T = 300\,\mathrm{K}$). The conduction band edge is shown in blue and the valence band edge in red. The Fermi level is represented by a dashed black line. (c) Si ion donor concentration and (d,e) simulated extrinsic electron density as a function of position from the nanowire core for a lattice temperature of 300 K.

where E_{w} and E_{v} are the terahertz transmitted electric fields through the nanowires and surrounding vaccum respectively, with * denoting a photoexcited state. The pump beam does not change the complex refractive index of the vacuum, so the electric fields E_{v}, E_{w} and $E_{\mathrm{w}*}$ can be written as:

$$E_{\mathrm{v}} = e^{in_{\mathrm{v}}\omega d/c} E_{\mathrm{i}} \tag{3}$$

$$E_{\mathrm{w}} = t_{\mathrm{vw}} t_{\mathrm{wv}} e^{in_{\mathrm{w}}\omega d/c} F P_{\mathrm{vwv}} E_{\mathrm{i}} \tag{4}$$

$$E_{\mathrm{w}*} = t_{\mathrm{vw}*} t_{\mathrm{w}*\mathrm{v}} e^{in_{\mathrm{w}*}\omega d/c} F P_{\mathrm{vw}*\mathrm{v}} E_{\mathrm{i}} \tag{5}$$

where t_{ij} are the Fresnel transmission coefficients, FP_{ijk} the Fabry-Pérot terms, c is the speed of light and $n_{\mathrm{w}*}$, n_{w} the refractive indices for the nanowires with and without photoexcitation respectively. By combining Equations 1 and 2, the ratio of terahertz fields for the nanowires with and without photoexcitation is given in terms of the OPTP measurement of $\frac{\Delta E}{E}$:

$$\frac{E_{\mathrm{w}*}}{E_{\mathrm{w}}} = \frac{\Delta E}{E}\left[1 + \left(\frac{1}{f_{\mathrm{w}}} - 1\right)\frac{E_{\mathrm{v}}}{E_{\mathrm{w}}}\right] + 1 \tag{6}$$

where $\Delta E = E_{\mathrm{on}} - E_{\mathrm{off}}$, the photoinduced change in transmission and $E = E_{\mathrm{off}}$, the THz transmission in the absence of photoexcitation. At THz frequencies, the thin film limit can be applied, as $\frac{n\omega\delta}{c} << 1$, so the approximation $\frac{E_{\mathrm{v}}}{E_{\mathrm{w}}} = 1$ can be made. By using this approximation, a parameter A can be defined:

$$A = \frac{E_{\mathrm{w}}}{E_{\mathrm{w}*}} = \frac{1}{\frac{1}{f_{\mathrm{w}}}\frac{\Delta E}{E} + 1} \tag{7}$$

By substituting in the appropriate FP_{ijk} and t_{ij} into Equation 3 and 4 and applying the thin film limit, the following equation is obtained:

$$\frac{E_{\mathrm{w}*}}{E_{\mathrm{w}}} = \frac{2 - \dfrac{i\omega d}{c}\left(1 + n_{\mathrm{w}}^2\right)}{2 - \dfrac{i\omega\, d}{c}\left(1 + n_{\mathrm{w}*}^2\right)} \tag{8}$$

Substituting in the general relation $n^2 = \epsilon$ to the above equation:

$$\epsilon_{\mathrm{w}*} = \left[-\frac{E_{\mathrm{w}}}{E_{\mathrm{w}*}}\left(2\frac{c}{i\omega d} - (1 + \epsilon_{\mathrm{w}})\right) + 2\frac{c}{i\omega d} - 1\right] \tag{9}$$

where $\epsilon_{\mathrm{w}*}$ and ϵw are the dielectric constants of the nanowires with and without photoexcitation respectively. The photoinduced conductivity, $\Delta\sigma$ is then given by:

$$\epsilon_{\mathrm{w}*} = \epsilon_{\mathrm{w}} + \frac{i\Delta\sigma}{\omega\epsilon_0} \tag{10}$$

where ϵ_0 is the permittivity of free space. Substituting Equation 9 into Equation 10, the photoinduced conductivity can be extracted:

$$\Delta\sigma = \epsilon_0\left(A - 1\right)\left[\frac{2c}{d} - i\omega\left(1 + \epsilon_{\mathrm{w}}\right)\right]. \tag{11}$$

Thus, using Equations 7 and 11, the photoinduced conductivity can be extracted from OPTP measurements using $\epsilon_{\mathrm{w}} = 12.95$ for bulk GaAs and values of f_{w} and d taken from optical electron microscope measurements.

Calculating the Photoexcited Carrier Density

The photoexcited carrier density, n_{p} for a sample of thickness d is given by:

$$n_{\mathrm{p}} = \frac{I}{Ed}\left(1 - e^{-d/\alpha}\right) \tag{12}$$

where I is the photoexcitation fluence, E is the photon energy and α is the absorption depth at the excitation wavelength. The absorption depth, $\frac{1}{\alpha}$ for GaAs is approximately 1μm for photons with energy 1.5 eV ($\lambda = 800\,$nm). This absorption depth is significantly larger than the nanowire diameter studied, so the nanowires fall within the thin film limit. Therefore, for a given photoexcitation intensity, the photoexcited carrier density is approximately constant for the nanowire diameter.

Fitting Process for Carrier Decay Traces and Conductivity Spectra

The charge carrier recombination dynamics for nanowires depend on excitation fluence and are described by the following carrier rate equation :

$$\frac{dn\,(t)}{dt} = -k_1 n - k_2 n^2 - k_3 n^3 \tag{13}$$

where N_d is the residual doping concentration, k_1 is the monomolecular recombination constant, describing the rate of mono-molecular processes, such as trap-assisted recombination, k_2 is the bimolecular recombination constant and k_3 is the rate for Auger recombination. This carrier rate equation was globally fitted to the experimental data at each temperature, by fixing the decay constants for each different excitation fluence for each sample. Similarly, for comparison, monoexponential fits for each temperature were carried out and gave similar values for the recombination constants and carrier lifetimes.

The fitting process is a nonlinear least-square fit that requires the following optimisation:

$$min_x||f\left(x\right)||^2 = min_x\left(f_1\left(x\right)^2 + f_2\left(x\right)^2 + ...f_n\left(x\right)^2\right). \tag{14}$$

The fitting process starts from an initial point and minimises the sum of the squares of the function described above. A lower bound of zero was placed on all the fitting parameters to make sure that they remain positive and therefore physical. The same fitting process was used to globally fit a Lorentzian conductivity response to the photoconductivity spectra with the doping density set as a global parameter for the undoped and doped sample respectively.

Calculation of Relative Radiative Efficiencies

The relative radiative efficiencies for the both the modulation and undoped sample were calculated from the PL spectra using the following method:

$$RE_{\text{sample}} = \frac{I_{\text{sample}}}{A_{\text{sample}}\left(\lambda_{\text{ext}}\right) \times \dfrac{I_{\text{p}}}{E_{\text{p}}}}. \tag{15}$$

where RE_{sample} is the radiative efficiency of the sample, I_{sample} is the integrated PL intensity of the sample, $A_{sample}\left(\lambda_{ext}\right)$ is the absorption of the sample at the photoexcitation wavelength and N_p is the photoexcited carrier density calculated from the photoexcitation fluence.

Normalised Photoconductivity Decays and Carrier Lifetimes for Modulation Doped and Undoped Reference Sample

Figure 3 in the main manuscript shows the change in nanowire conductivity as a function of time after photoexcitation for the modulation doped and undoped reference sample respectively for a range of temperatures between 5 K and 300 K. For all temperatures, the normalised photoconductivity shows a sharp rise on the order of 1 ps of photoexcitation followed by a slow, monoexponential decay for both samples. For the doped sample, at temperatures 5 K and 30 K, the carrier decay traces clearly coincide with each other and possess similar photoconductivity lifetimes. However, for temperatures above 30 K, longer photoconductivity decays are observed, with the photoconductivity lifetime clearly increasing with increasing temperature. For both samples, monoexponential behaviour was observed. At the excitation fluences used in this work the values of n were low enough that both bimolecular and Auger recombination rates were found to be negligible and thus the monomolecular recombination rate, k_1, could be determined by fitting a monoexponential to the photoconductivity decays. Therefore the photoconductivity lifetimes in Figure 2(c,d) in the manuscript were fitted with a monoexponential to extract the photoconductivity lifetimes. This monoexponential behaviour has previously been observed and is attributed to trap-assisted recombination in GaAs nanostructures.[3,4]

The calculated photoconductivity lifetimes for both the modulation doped and undoped reference samples are displayed in the inset of Figure 2(c,d) of the main manuscript. A clear increase in the photoconductivity lifetime is observed, from 810 ± 68 ps at 5 K to 2.13 ± 0.18 ns at 300 K, for the modulation doped sample. This is in stark contrast to the carrier lifetimes for the undoped reference sample, which were found to decrease slightly with increasing temperature, from 1.73 ± 0.15 ns to 1.09 ± 0.09 ns. This decrease in carrier lifetime is expected for undoped semiconductor nanostructures, due to bandgap narrowing

and increased trap-assisted recombination with increasing temperature. However, for the modulation doped sample, a sharp rise in the carrier lifetime can be seen above 50 K in the inset of Figure 2d of the main manuscript. We attribute this sharp rise to ionisation of the Si dopants in the AlGaAs layer. This agrees with the theoretical value for the ionisation energy of Si dopants in bulk AlGaAs, $\sim 6\,\mathrm{meV}$,[5] coinciding with an ionisation temperature of $\sim 50\,\mathrm{K}$. As the Si donors are ionised, the liberated electrons migrate into the potential well of the nanowire core and passivate trap states at the GaAs/AlGaAs core-shell interface, thereby prolonging the carrier lifetime. Thus, the onset of this passivation effect due to modulation doping coincides with the ionisation temperature of the Si dopants and can clearly be seen in the nanowire photoconductivity decay traces. As shown in the inset of Figure 2d of the main manuscript, at room temperature ($T = 300\,\mathrm{K}$), the carrier lifetime for the modulation doped sample is over a factor of 2 higher than for the undoped sample, highlighting an advantage of modulation doping for use in room temperature optoelectronic devices.

Photoconductivity Spectra as a Function of Frequency and Photoexcitation Fluence for Doped and Undoped Sample

Figure S2 and S3 show colour plots of the real and imaginary component of the photoconductivity as a function of frequency and photoexcitation fluence respectively. A clear red-shift can be seen in the resonant frequency, which is displayed by the white line in the imaginary component (i.e. where it passes through zero). This red-shift is expected for plasmon modes, where the resonant frequency scales with the square root of the carrier density, as shown in Figure S4. This relationship has previously been demonstrated for modulation doped and undoped GaAs/AlGaAs nanowires.[2]

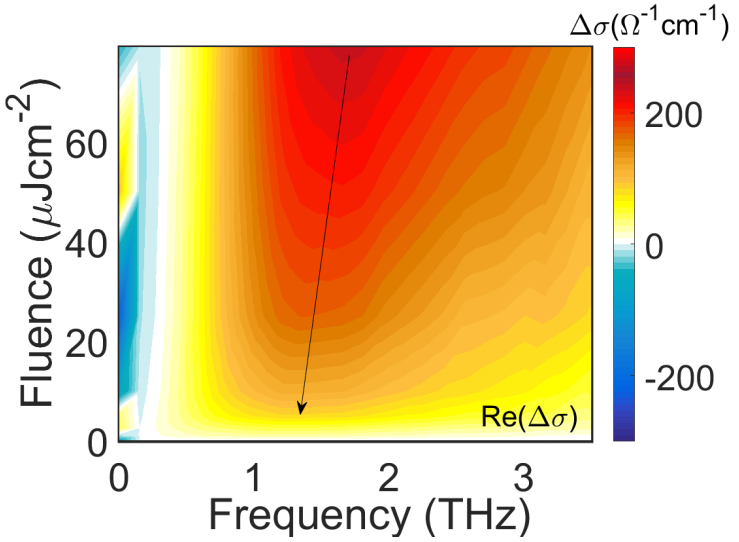

Figure S2: Colour plot of the real component of the photoconductivity as a function of frequency and photoexcitation fluence. Arrow depicts position of resonant frequency.

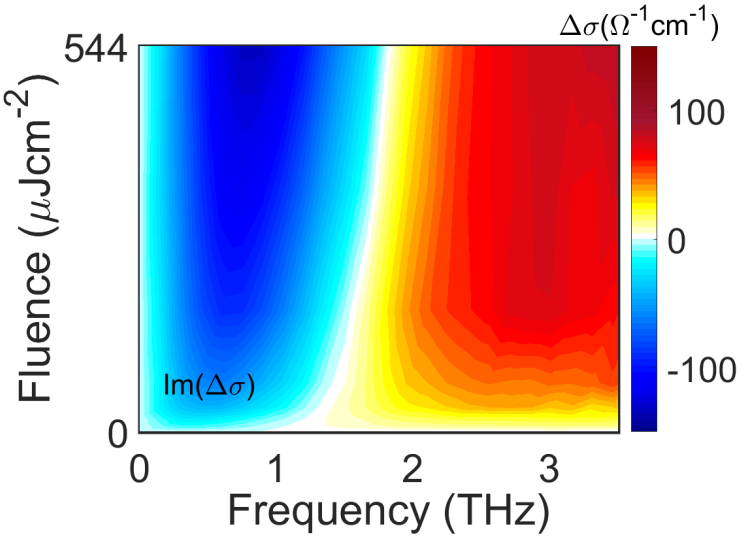

Figure S3: Colour plot of the imaginary component of the photoconductivity as a function of frequency and photoexcitation fluence. White line depicts position of resonant frequency.

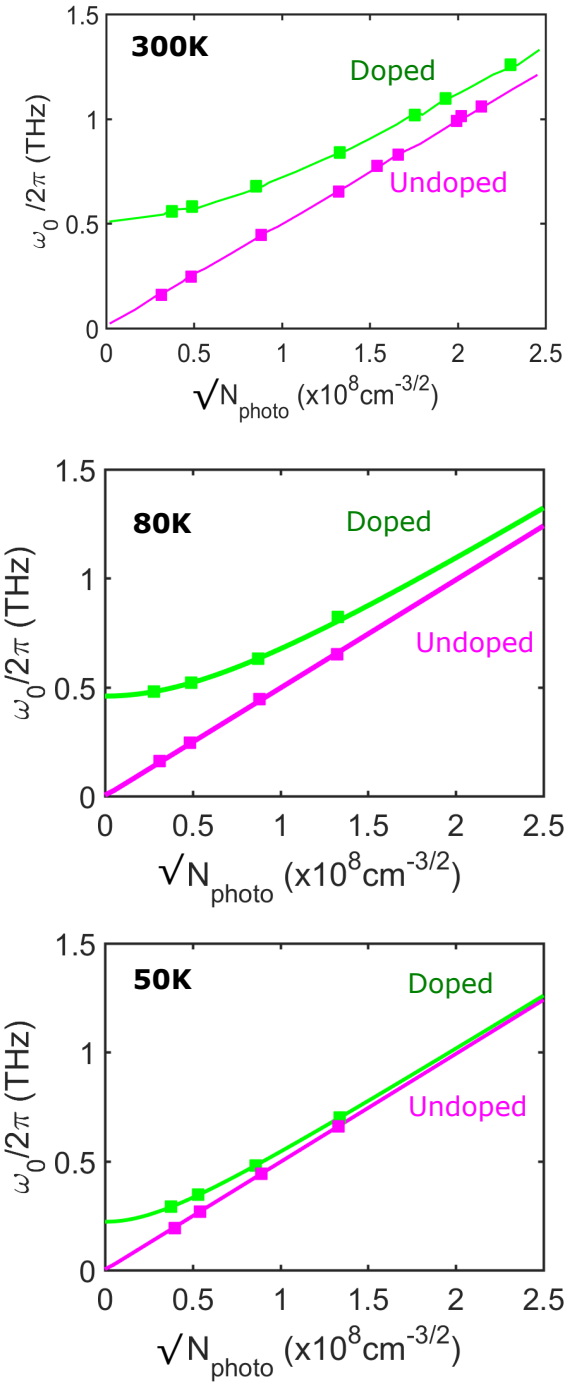

Figure S4: Plot of plasma frequency against the square root of the charge carrier density for the doped (green) and undoped (pink) nanowires at room temperature and 80K.

Normalised PL Spectra for the Doped and Undoped Nanowires

Figure S5 and Figure S6 show the normalised photoluminescence spectra as a function of emission energy and temperature for both the doped and undoped nanowires. For both the doped and undoped samples, a clear red shift in the PL peak position is seen above 50 K due to bandgap narrowing following the Varshni equation. Above this temperature, the PL behaviour transitions between excitonic to electron-hole plasma, as excitons are thermally activated. Below 50 K, for the doped sample, two peaks can clearly be seen, with the higher energy peak attributed to bandgap emission and the lower energy peak to Type-II recombination across WZ-ZB segments within the nanowire. For the undoped sample, the same two peaks are also observed, but the lower energy peak is reduced in intensity and the spectrum appears broader due to a lower defect density in the undoped reference nanowires.

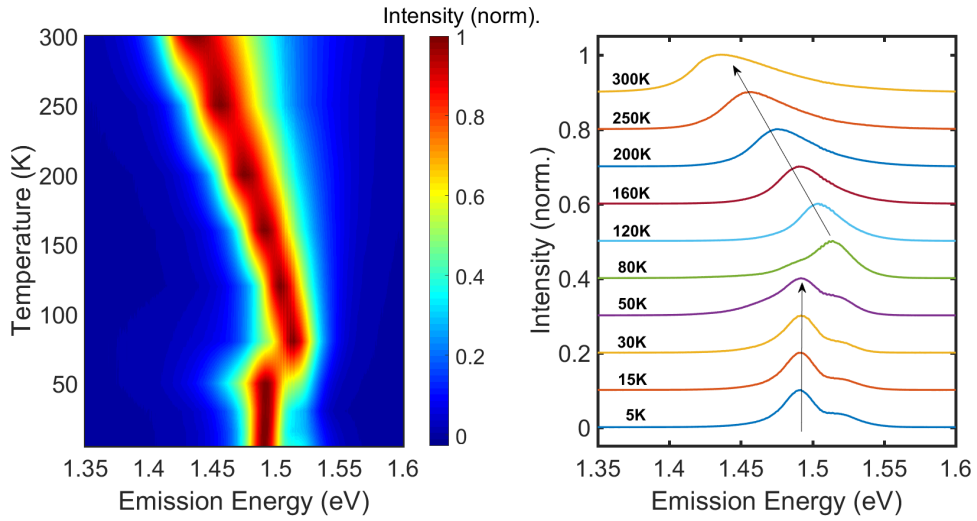

Figure S5: Colour map and normalised PL spectra as a function of emission energy and temperature for the doped nanowires.

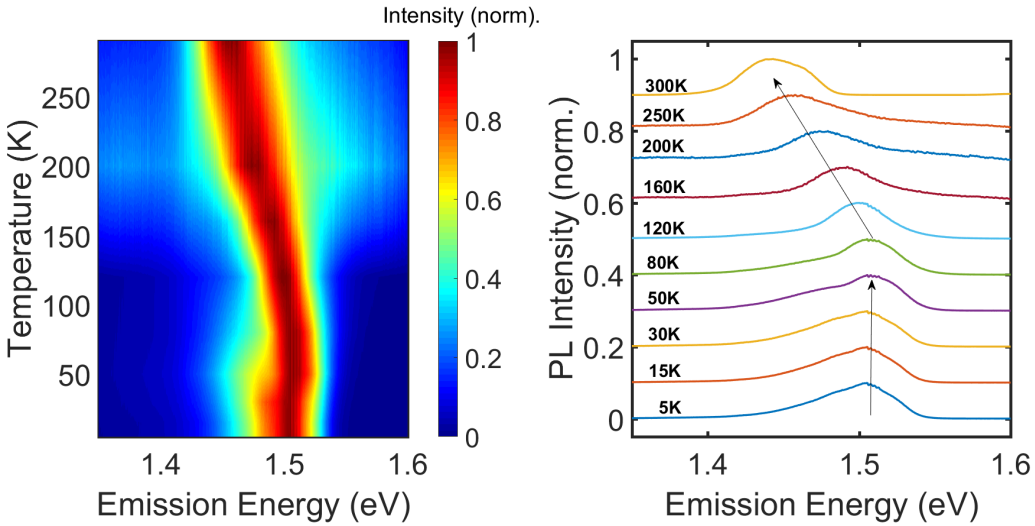

Figure S6: Colour map and normalised PL spectra as a function of emission energy and temperature for the undoped nanowires.

Fluence Dependence of PL Spectra as a Function of Temperature for Doped and Undoped Samples

Figure S7 shows the normalised PL spectra as a function of emission energy for both the modulation doped and undoped nanowires at a range of fluences between 15 μJ cm^{-2} and 500 μJ cm^{-2} for temperatures between 5 K and 300 K. Four temperatures of 5 K, 50 K, 120 K and 300 K are presented, with schematic diagrams of the bandedge for the ZB/WZ segments as insets in the figure. For both samples, a clear Moss-Burstein shift[6] is seen with increasing fluence at temperatures below 50 K. Two peaks are seen in the PL spectra at 1.49 eV (labelled 2), which coincides to recombination from electrons in the ZB segment with holes in the WZ segment and 1.52 eV (labelled 1), which corresponds to bandgap recombination. The difference between these two peaks is $\sim$ 30 meV, which agrees with literatures values for the band offset of wurzite GaAs.[7–10] As fluence is increased and thereby the number of photoexcited electrons and holes are increased, the wells created by the ZB/WZ segments become saturated and recombination across the ZB/WZ segment (peak 2) becomes higher in energy and therefore blue-shifts. At high fluences and high temperatures above 5 K, the well

becomes completely saturated and only bandgap recombination (peak 1) can be seen. For the undoped reference sample, which has a much lower radiative efficiency, the PL spectra are very broad. The recombination due to the type II band alignment (peak 2) is also reduced, as less crystal defects are observed in the undoped nanowires. This can be seen from a comparison of the TEM images in Figure S7b & f, where the modulation doped nanowires show $\sim 50\,\text{defects}/\mu\text{m}$ and the undoped nanowires possess $\sim 30\,\text{defects}/\mu\text{m}$. For the doped nanowires, the type II recombination across the ZB/WZ segment (peak 2), is therefore much more pronounced. This peak is no longer observed above 50 K, as the dopants are ionised and aid to saturate the wells produced by the crystal defects, so that only bandgap recombination is observed. Thus, in the colour maps of the PL spectra as a function of temperature, the sharp blue shift, coinciding with ionisation temperature, is seen as an effect of increased crystal defects and donor ionisation in the modulation doped nanowires. It is proposed that for pure phase GaAs nanowires, such a shift would not be observed. However, for the purpose of our study, it aids in confirming the validity of the activation energies extracted from THz measurements.

Temperature Dependence of the Full Width Half Maximum for Doped and Undoped Samples

Figure S8 shows the full width half maxima plotted as a function of temperature for both the doped and undoped GaAs/AlGaAs nanowires. For the modulation doped nanowires, it is clear that the temperature dependence of the full width half maximum is predominantly due to LO phonon scattering, where for the undoped sample, it is dominated by impurity scattering. The data was fitted with the following equation to detemine the contributions of each scattering mechanism:

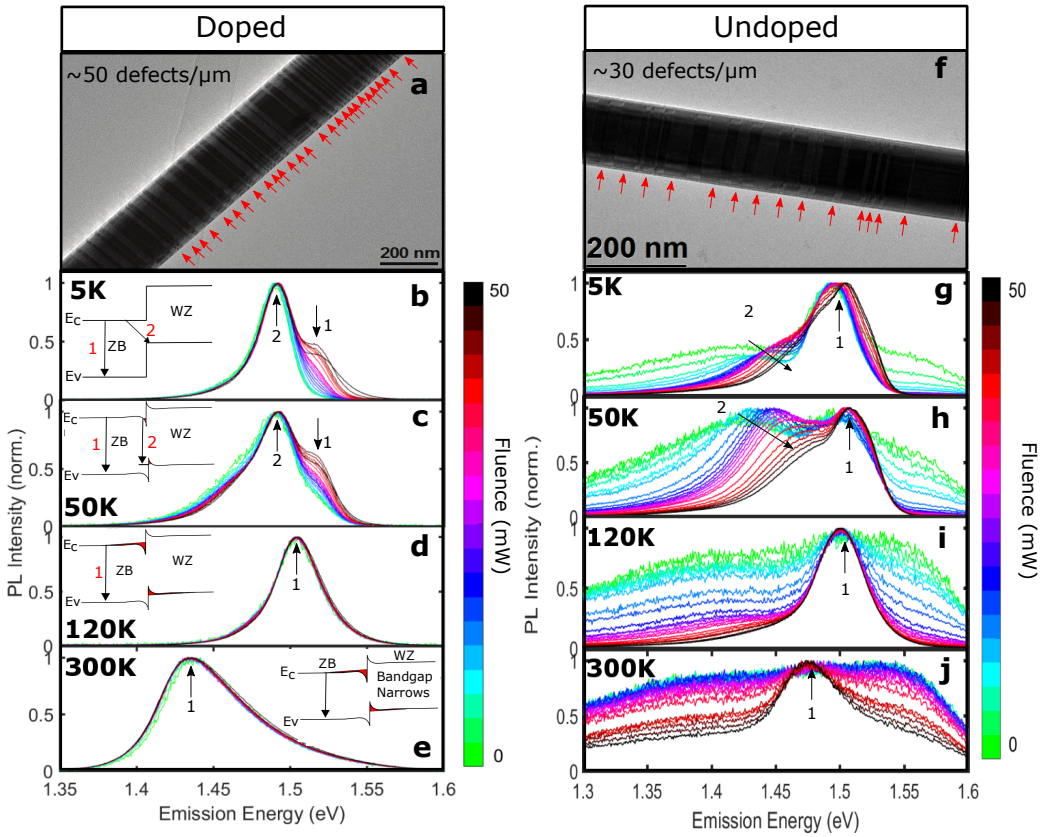

Figure S7: High-resolution STEM images of the modulation doped (a) and undoped (f) GaAs/AlGaAs nanowires. Photoluminescence spectra as a function of emission energy and fluences between $150\mu W$ and $50\mu W$ at temperatures of 5 K, 50 K, 120 K and 300 K for the modulation doped (b-e) and undoped (g-j) nanowires.

$$\Gamma(T) = \Gamma_0 + \gamma_a T + \gamma_{LO} N_{LO}(T) + \gamma_{imp} e^{-\frac{E_b}{k_b T}}, \tag{16}$$

where Γ_0 is temperature-independent inhomogeneous broadening term, arising from disorder and imperfections; the second and third terms are homogeneous broadening terms due to acoustic deformation and longitudinal optical phonon scattering respectively; and the fourth term is due to impurity scattering, where E_b is the ionisation energy of the impurities. For the acoustic term, a linear dependence is assumed, as their energy is much smaller than $k_b T$ for this observation range. The longitudinal optical phonon term is given by the Bose-Einstein distrubtion, with $N_{LO} = 1/\left(e^{E_{LO}/k_b T} - 1\right)$ and E_{LO} representing the energy of a typical LO phonon branch.[11] γ_a, γ_{LO} and γ_{imp} are the respective phonon-coupling strengths for each scattering mechanism.

For the modulation doped sample, the terms due to acoustic phonons were found to be negligible, with the dominant scattering mechanism found to be due to LO phonon scattering, with a coupling strength of 17 meV and an LO phonon energy of 25.6 ± 7 meV. For the undoped sample, the acoustic term was again found to be negligible, with the dominant scattering mechanism now be due to background impurity scattering, with a coupling strength of 5.3 meV. The ionisation was taken as 6.72 meV, from the THz spectral data. Thus, comparisons of the linewidth clearly show a different temperature dependence for the doped and undoped sample, with the modulation doping clearly reducing impurity scattering within the nanowire.

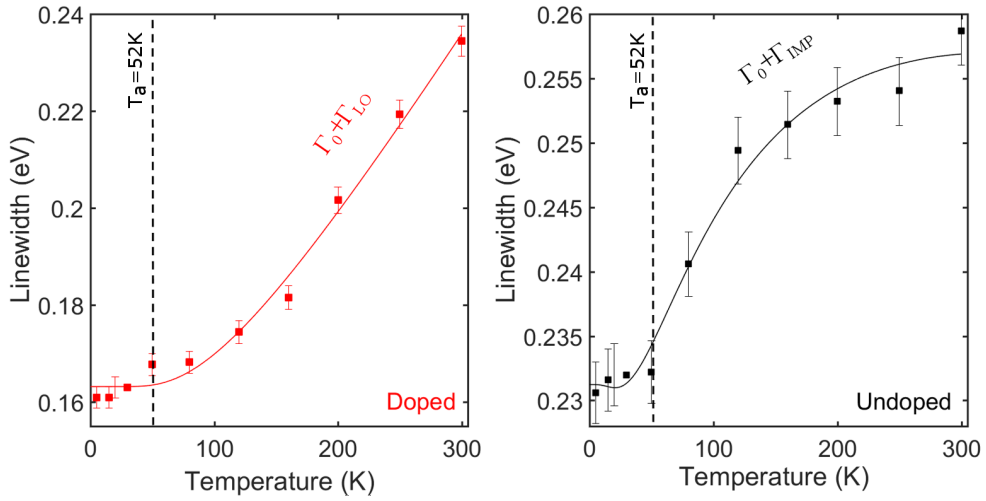

Figure S8: Colour map and normalised PL spectra as a function of emission energy and temperature for the undoped nanowires.

Comparison of Bandgap Emission from Experimental Data to Simulations

Figure S9 shows the comparison of the peak position of the PL bandgap emission to calculated bandgap emission energies taken from NextNano simulations as a function of temperature. The emission energies from the simulation are calculated using the Varshni equation and it is assumed that the nanowires possess a pure zinc-blende crystal structure. It can be seen for the doped sample, that higher energy peak does indeed follow the same relationship with temperature as for NextNano simulations, with a slight deviation due to crystal structure defects. The lower energy peak, however deviates from the Varshni relationship, displaying a Moss-Burstein shift, inherent to Type-II recombination across WZ-ZB segments. For the undoped sample, the bandgap emission also follows the Varhsni relationship, with the peak emission energy taking an average value in between the high and low energy peaks for the doped sample, due to its broader PL spectrum.

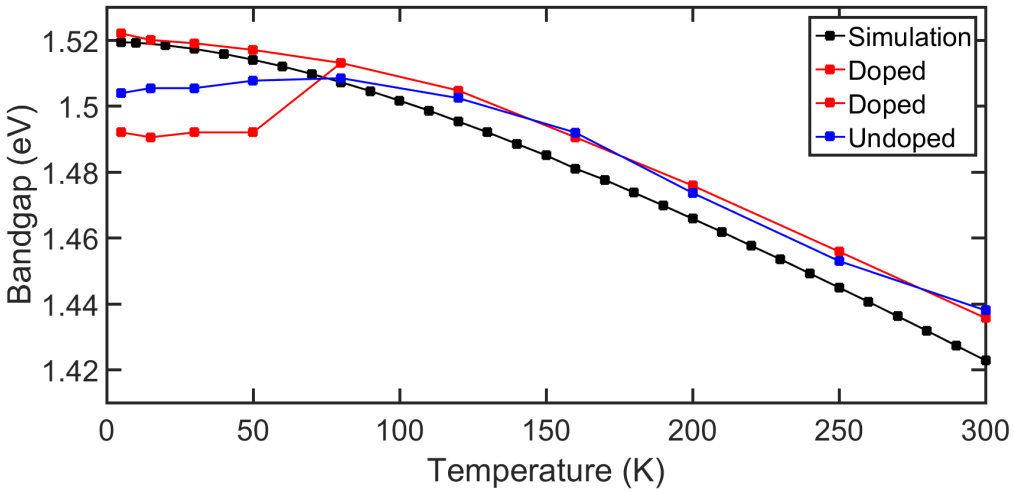

Figure S9: Peak emission energies from PL spectra as a function of temperature for the doped and undoped nanowires, compared to NextNano simulations.

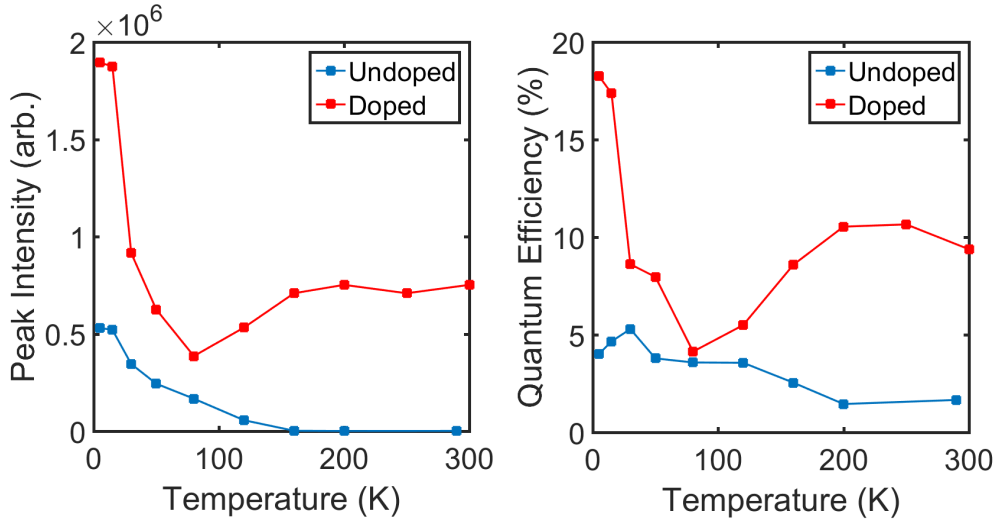

Figure S10: Peak PL intensity and radiative efficiency as a function of temperature for the doped and undoped nanowires.

Comparison of PL Peak Intensity as a Function of Temperature for Doped and Undoped Samples

Figure S10 shows the comparison of the PL peak intensity, as well as the relative radiative efficiency as a function of temperature for both the undoped and doped nanowires. The PL peak intensity is directly related to relative radiative efficiency. For the undoped sample, both the PL peak intensity and radiative efficiency decreases with increasing temperature, however, for the doped sample an increase in peak intensity and radiative efficiency is seen with increasing temperature above 50 K. This increase in intensity and radiative efficiency is a direct result of passivation of trap states at the core-shell interface due to modulation doping.

Detailed Description of Mechanisms Affecting Radiative Efficiency at Low Temperatures

For both the modulation doped and undoped nanowires, the radiative efficiencies were extracted at the highest fluence of $500\,\mu\mathrm{J\,cm^{-2}}$ for a range of temperatures between 5 K and 300 K and are plotted in the main manuscript in Figure 4b. At the lowest temperature of 5 K, the radiative efficiency was found to be at a maximum of $5.3 \pm 0.4\%$ and $18.3 \pm 2.3\%$ for the undoped and doped nanowires respectively. For both samples, an increase in radiative efficiency is observed below 50 K, which is attributed to the formation of excitons, as the exciton binding energy in GaAs is 4.2 meV (T = 48 K).[12–14] Below 50 K, it has been found for undoped GaAs/AlGaAs core-shell nanowires that there is an enhancement in thermal detrapping of bound excitons with increasing temperature, allowing them to be directly activated into the free exciton continuum and suppress radiative recombination. For the modulation doped sample, this effect is increased with a much sharper increase in radiative efficiency with decreasing temperature observed. This is attributed to an increase in defects

in the doped nanowire, leading to an increase in bound exciton population, as can be seen in Figure S7, where the intensity of the lower energy PL peak due to bound excitons is significantly increased in comparison to the undoped reference. This increase in bound exciton population enhances the effect of thermal detrapping and thereby the increase in radiative efficiency seen at 5 K for the modulation doped sample. For temperatures above 50 K, a decrease in radiative efficiency with increasing temperature is seen for the undoped reference nanowires, due to thermal activation into a metastable state, leading to non-radiative recombination, which surpresses radiative efficiency. In stark contrast, the modulation doped sample displays an increase in radiative efficiency with increasing temperature above 50 K. Above this temperature, the Si donors in the AlGaAs shell become ionised and the donated electrons passivate trap states at the GaAs/AlGaAs interface. This allows for the increasing free electron concentration to avoid being trapped at the interface and thereby radiatively recombine and the radiative efficiency to increase. At room temperature, a high radiative efficiency of $9.4 \pm 1.2\%$ is seen, an order of magnitude higher than for the undoped sample. This is an exciting result, as it suggests that the increase in radiative efficiency at room temperature for the doped nanowires is a direct result of passivation of trap states, which may be achieved through well designed modulation doping. Recently, p-doping in GaAs nanowires has also shown to increase radiative efficiency in unpassivated nanowires, allow for nanowire lasing to be achieved at room temperature.[15] Thus, doped nanowires are promising candidates for use in optoelectronic devices, such as nanolasers and LEDs, owing to their excellent radiative performance at both low and high temperatures.

References

(1) Birner, S.; Zibold, T.; Andlauer, T.; Kubis, T.; Sabathil, M.; Trellakis, A.; Vogl, P. *IEEE Transactions on Electron Devices* **2007**, *54*, 2137–2142.

(2) Boland, J. L.; Conesa-Boj, S.; Parkinson, P.; Tütüncüoglu, G.; Matteini, F.; Rüffer, D.;

Casadei, A.; Amaduzzi, F.; Jabeen, F.; Davies, C. L.; Joyce, H. J.; Herz, L. M.; Fontcuberta i Morral, A.; Johnston, M. B. *Nano Letters* **2015**, *15*, 1336–1342.

(3) Boland, J. L.; Conesa-Boj, S.; Tütüncouglu, G.; Matteini, F.; Rüffer, D.; Casadei, A.; Gaveen, F.; Amaduzzi, F.; Parkinson, P.; Davies, C.; Joyce, H. J.; Herz, L. M.; Morral, A. F.; Johnston, M. B. Terahertz Spectroscopy of Modulation Doped Core-Shell GaAs/AlGaAs Nanowires. 40th International Conference on Infrared, Millimeter, and Terahertz waves (IRMMW-THz). 2015.

(4) Joyce, H. J.; Docherty, C. J.; Gao, Q.; Tan, H. H.; Jagadish, C.; Lloyd-Hughes, J.; Herz, L. M.; Johnston, M. B. *Nanotechnology* **2013**, *24*, 214006.

(5) Watanabe, M.; Maeda, H. *Japanese Journal of Applied Physics* **1984**, *23*, L734–L736.

(6) Grundmann, M. *The Physics of Semiconductors*; Springer, 2006.

(7) Ahtapodov, L.; Todorovic, J.; Olk, P.; Mjåland, T.; Slåttnes, P.; Dheeraj, D. L.; Van Helvoort, A. T. J.; Fimland, B. O.; Weman, H. *Nano Letters* **2012**, *12*, 6090–6095.

(8) Kusch, P.; Breuer, S.; Ramsteiner, M.; Geelhaar, L.; Riechert, H.; Reich, S. *Physical Review B - Condensed Matter and Materials Physics* **2012**, *86*, 075317.

(9) Spirkoska, D.; Efros, A. L.; Lambrecht, W. R. L.; Cheiwchanchamnangij, T.; Fontcuberta I Morral, A.; Abstreiter, G. *Physical Review B - Condensed Matter and Materials Physics* **2012**, *85*, 045309.

(10) Heiss, M.; Conesa-Boj, S.; Ren, J.; Tseng, H. H.; Gali, A.; Rudolph, A.; Uccelli, E.; Peir, F.; Morante, J. R.; Schuh, D.; Reiger, E.; Kaxiras, E.; Arbiol, J.; Fontcuberta I Morral, A. *Physical Review B - Condensed Matter and Materials Physics* **2011**, *83*, 045303.

(11) Wright, A. D.; Verdi, C.; Milot, R. L.; Eperon, G. E.; Pérez-Osorio, M. A.; Snaith, H. J.; Giustino, F.; Johnston, M. B.; Herz, L. M. *Nature Communications* **2016**, *7*, 11755.

(12) Ryan, J.; Taylor, R.; Turberfield, A.; Maciel, A. *Physical Review Letters* **1984**, *53*, 1841–1844.

(13) Gurioli, M.; Vinattieri, A.; Colocci, M. *Phys. Rev. B* **1991**, *44*, 3115–3124.

(14) Vilms, J.; Spicer, W. E. *Journal of Applied Physics* **1965**, *36*, 2815–2821.

(15) Burgess, T.; Saxena, D.; Mokkapati, S.; Li, Z.; Hall, C. R.; Davis, J. A.; Wang, Y.; Smith, L. M.; Fu, L.; Caroff, P.; Tan, H. H.; Jagadish, C. *Nature Communications* **2016**, *7*, 11927.